Boundary Layer Evolution within a Canyonland Basin. Part II: Numerical Simulations of Nocturnal Flows and Heat Budgets

JEROME D. FAST, SHIYUAN ZHONG, AND C. DAVID WHITEMAN

Pacific Northwest National Laboratory, Richland, Washington

(Manuscript received 11 December 1995, in final form 12 April 1996)

ABSTRACT

A mesoscale model is used to simulate the nocturnal evolution of the wind and temperature fields within a small, elliptical basin located in western Colorado that has a drainage area of about 84 km^2. The numerical results are compared to observed profiles of wind and potential temperature. The thermal forcing of the basin wind system and the sources of air that support the local circulations are determined. Individual terms of the basin atmospheric heat budget are also calculated from the model results.

The model is able to reproduce key features of the observed potential temperature profiles over the basin floor and winds exiting the basin through the narrow canyon that drains the basin. Complex circulations are produced within the basin atmosphere as a result of the convergence of drainage flows from the basin sidewalls. The strength of the sidewall drainage flow varies around the basin and is a function of the source area above the basin, the local topography, and the ambient winds. Flows on the basin floor are affected primarily by the drainage winds from the northern part of the basin. The near-surface sidewall drainage flows converge within the southern portion of the basin, producing a counterclockwise eddy during most of the evening. Evaluation of the individual terms of the atmospheric heat budget show that the forcing due to advection and turbulent diffusion is significantly larger above the sidewalls than over the basin floor; therefore, measurements made over the basin floor would not be representative of the basin as a whole. The cooling in the center of the basin results from the local radiative flux divergence and the advection of cold air from the sidewalls, and the cooling above the basin sidewalls is due primarily to turbulent sensible heat flux divergence. A high rate of atmospheric cooling occurs within the basin throughout the evening, although the strongest cooling occurs in the early evening hours. Sensitivity tests show that the thermal structure, circulations, and rate of cooling can be significantly affected by ambient wind direction and, to a lesser extent, vegetation coverage.

1. Introduction

In a companion paper, Whiteman et al. (1996, hereafter referred to as W96) evaluated the mass, heat, and moisture budgets for an atmospheric control volume in Colorado's Sinbad Basin from tethered balloon observations and surface measurements during a 16.5-h period beginning at 1800 mountain standard time (MST) 15 July 1988. A high rate of atmospheric cooling continued in this basin throughout the entire night that was attributed primarily to turbulent sensible heat flux divergence and, to a lesser extent, radiative flux divergence.

Several unexpected features appeared in their analysis. One unexpected feature was the large discrepancy between the sensible heat flux divergence from the basin control volume, calculated as a residual of the atmospheric heat budget, and the sensible heat flux divergence estimated from surface energy budget measurements on the basin floor. The heat budget analysis indicated that a large sensible heat flux divergence must occur from the basin control volume during nighttime, but the observations showed that there was no appreciable downward turbulent sensible heat flux at the basin floor. Another unexpected feature was the observation of large mass fluxes through the narrow exit canyon. The Sinbad Basin was selected for the field experiment partially because it was assumed that the basin outflow would be weak; however, the mass fluxes were comparable to fluxes observed in well-drained valleys.

W96 assumed that the strong nocturnal cooling within the basin was caused by enhanced downward turbulent sensible heat fluxes over the basin sidewalls associated with downslope drainage flows and that the flow through the canyon was the result of a large horizontal pressure gradient that developed between the basin and its surroundings due to stronger cooling within the basin. Unfortunately, no observations were available on the basin sidewalls or at other locations outside of the basin to provide direct evidence to support these hypotheses. Understanding these features re-

Corresponding author address: Dr. Jerome D. Fast, Battelle, Pacific Northwest National Laboratory, P.O. Box 999, MSIN K9-30, Richland, WA 99352.
E-mail: jd_fast@pnl.gov

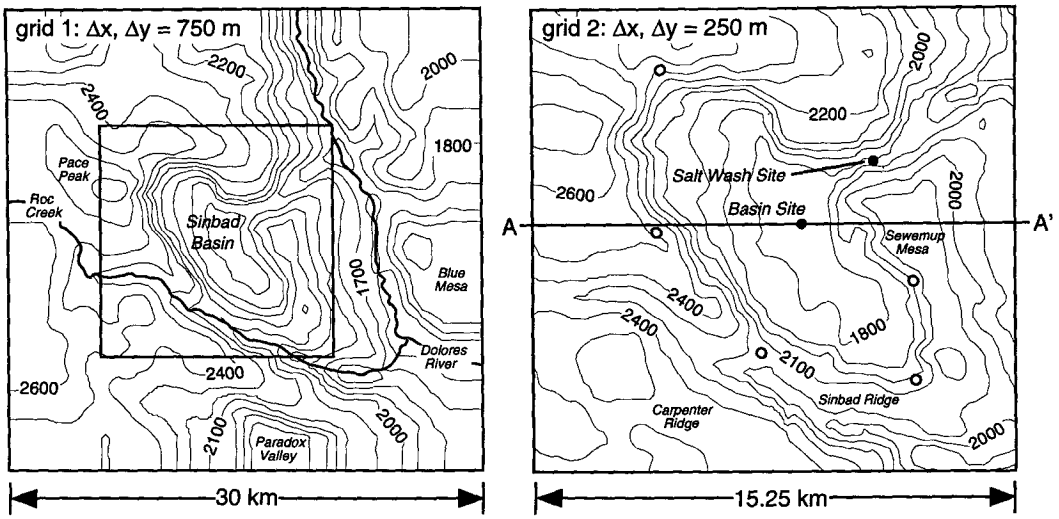

FIG. 1. Topography employed by the mesoscale model on (a) grid 1 and (b) grid 2 along with the locations of tethersonde and airsonde measurements taken at the basin and Salt Wash sites (filled circles) and tracer release locations used by the dispersion model (open circles).

quires measurements at many different sites, a difficult and expensive proposition for most basins or valleys. On the other hand, these features can easily be examined by dynamic models that can resolve the sloping sidewalls of the basin. Numerical experiments are capable of providing a new understanding of basin heat budgets because datasets obtained from models represent dynamically balanced realizations of the flows.

A high-resolution three-dimensional mesoscale numerical model is used in this study to simulate the evolution of the thermally driven flow system in the Sinbad Basin for the case presented in W96. The predicted wind and temperature profiles are compared to the tethersonde observations. The wind and temperature fields at other locations are presented to illustrate the complexity of the flows, behavior of the sidewall drainage flows, and preferential flow patterns resulting from topographic forcing that may develop within the basin. The mechanisms responsible for the strong winds within the narrow canyon will also be addressed. As described by W96, several assumptions are required to obtain the individual terms of the heat budget using observational data. However, assumptions regarding closure of the heat budget are not necessary in this numerical modeling study. The terms of the heat budget equation are calculated three-dimensionally during the evolution of the nocturnal boundary layer to provide information regarding the role of slope flows on the basin heat budget. Some of the assumptions employed by W96 will be addressed by examining individual terms of the simulated heat budget. A Lagrangian particle dispersion model is also used in this study to depict the circulations within the basin so that characteristics of the drainage flows can be better understood. Moreover, this numerical modeling study will investigate the effect of large-scale ambient winds and surface characteristics on the slope flows and the basin heat budget.

The mesoscale model and the dispersion model are described in section 2. Section 3 describes the numerical experiments, and section 4 compares some of the model results with observations. Section 5 discusses the temperature fields and the basin energy budget further, and section 6 presents the conclusions of this study.

2. Model description

a. Atmospheric model

The Regional Atmospheric Modeling System (RAMS, version 3a) described by Pielke et al. (1992) is used to predict the small-scale flows within and around the Sinbad Basin. In this study, the turbulence parameterization consists of a level 2.5 closure scheme with a prognostic turbulence kinetic energy equation as proposed by Mellor and Yamada (1982) and modified for the case of growing turbulence according to Helfand and Labraga (1988). Since cloud processes are not important for this case, the cumulus and microphysical parameterizations are not activated, so that water vapor is treated as a passive scalar. The Mahrer and Pielke (1977) shortwave parameterization and the Chen and Cotton (1983) longwave parameterization are used to determine the heating or cooling due to radiative fluxes. A prognostic soil–vegetation module calculates the diurnal variations of temperature and moisture at the ground–atmospheric interface. Albedo, emissivity, leaf-area index, fractional coverage, roughness length, displace-

TABLE 1. Summary of numerical experiments.

Name	Initial wind profile	Surface characteristics
Primary experiments:		
1	Grand Junction sounding and basin site tethersonde at 0000 UTC 15 July 1988	Uniform vegetation type—desert shrub; uniform soil type—loamy sand
2	Same as experiment 1 except wind speed set to 0.1 m s^{-1}	Same as experiment 1
Sensitivity experiments:		
3	Same as experiment 1	Uniform vegetation type—desert; uniform soil type—loamy sand
4	Same as experiment 1	Mixed vegetation type—desert and desert shrub; mixed soil type—loamy sand and clay
5	Same as experiment 1 except northwest wind direction within 3.3 km of basin floor	Same as experiment 1
6	Same as experiment 1 except southeast wind direction within 3.3 km of basin floor	Same as experiment 1
7	Same as experiment 1 except northeast wind direction within 3.3 km of basin floor	Same as experiment 1

ment height, and root fraction all depend upon the type of vegetation. The Biosphere–Atmosphere Transfer Scheme (BATS) vegetation classifications (Dickinson et al. 1986) are used. Turbulent sensible heat, latent heat, and momentum fluxes in the surface layer are then based on similarity equations (Louis 1979). Eleven soil levels are used down to a depth of 1 m below the surface with a variable grid spacing.

The nested grid configuration employed to resolve the small-scale flows within and around Sinbad Basin is shown in Fig. 1. A horizontal grid spacing of 750 and 250 m is used for grids 1 and 2, respectively. The topography for both grids is derived from a 3″ (about 90 m) terrain dataset and is then smoothed with a silhouette-averaging scheme that preserves realistic topographic heights. Both grids employ a stretched, vertical, terrain-following coordinate with a grid spacing of 30 m near the surface that increases to 1000 m near the model top at an elevation of 12.4 km mean sea level (MSL). Due to the staggered coordinate system, the lowest grid point is located about 12.5 m above ground level (AGL). With this vertical resolution, 14 grid points are positioned within 1000 m of the ground to resolve the nocturnal slope flows. While the horizontal grid spacing in this study is smaller than many mesoscale model applications, RAMS has been shown to reproduce many observed characteristics of flows in complex terrain (Fast 1995; Poulos and Bossert 1995) using grid spacings slightly larger than most large-eddy simulation studies.

As seen in Fig. 1, the Sinbad Basin is an elliptical basin that has only one exit, the deep and narrow Salt Wash Canyon. The Salt Creek flows through the Salt Wash Canyon and empties into the Dolores River that runs from south to north through the eastern portion of the domain (Fig. 1a). Roc Creek flows down the narrow valley just south of the basin between Sinbad Ridge and Carpenter Ridge (Fig. 1b). Since the terrain elevations are generally higher in the western portion of the domain, westerly nocturnal drainage winds may develop and flow into the lower terrain around the Dolores River when the synoptic forcing is weak. The strength and direction of these drainage winds are expected to be affected by the Sinbad Basin and the other small-scale terrain features in the area. It should be noted that the Salt Wash Canyon entrance in the model (Fig. 1b) is wider and smoother than the actual entrance given on topographic maps (W96) because the 3″ terrain data does not resolve this feature well. Two observation sites (the basin and Salt Wash sites) are also shown in Fig. 1b.

b. Dispersion model

A Lagrangian particle dispersion model (LPDM) described by Fast (1995) is used to illustrate the behavior of the nighttime drainage flows within the Sinbad Basin. Atmospheric dispersion is simulated by tracking a large number of particles in which trajectories are based on the mean velocity components produced by RAMS and subgrid-scale turbulent velocity components. The subgrid-scale turbulent velocities are computed by solving the Langevin equation by a Markov chain formulation (Legg and Raupach 1982). The turbulent velocities are a function of the Lagrangian timescale, and the turbulent velocity statistics are consistent with the second-order closure applied in RAMS. Particles are assumed to be nonbuoyant, and a perfect reflection of particles is assumed to occur at the ground.

The mean velocity field employed by LPDM is based on output produced by RAMS at 30-min intervals. LPDM linearly interpolates the mean velocity field in time during individual 30-min periods using a time step of 5 s. Particles are released continuously between 1900

and 0500 MST from five locations along the basin sidewalls (Fig. 1b) to illustrate the flow patterns, to track air parcels originating from different slopes, and to determine the amount of mixing within the basin. Particle concentration is then calculated by grid-cell averaging within grid 2 (Fig. 1b) using a horizontal grid spacing of roughly 125 m.

3. Experimental design

The simulations performed to examine the nocturnal flows and the heat budget within the Sinbad Basin are summarized in Table 1. The initial conditions for the control simulation (experiment 1) shown in Fig. 2 are assumed to be horizontally homogeneous and are based on a combination of the observations taken from an airsonde at the basin site and the rawinsonde sounding from Grand Junction, Colorado, (80 km to the northeast) at 0000 UTC (1700 MST) 15 July 1988. Wind and temperature measurements from the airsonde are used up to approximately 1 km above the basin rim, and values from the Grand Junction sounding are used above that level. The vegetation type is specified as desert shrub and the soil type is specified as sandy loam over the entire domain. The initial soil temperature profile for each column of soil grid points is set equal to the measured profile at the basin floor at 1600 MST (W96) so that the temperature 1 m below the surface is 23°C. The initial vegetation temperature is set equal to the atmospheric temperature at the lowest model grid point. W96 found that latent heat fluxes were negligible within the arid Sinbad Basin for this period; therefore, the initial soil moisture is set equal to a dry value (15% of saturation) throughout the domain. A 12-h forecast is then made using radiation lateral boundary conditions and a time step of 7.5 and 2.5 s on grids 1 and 2, respectively.

Experiments 2–6 are similar to the control simulation, except in the treatment of the surface characteristics or the initial wind profile. An initial wind speed of 0.1 m s^{-1} is used throughout the domain in experiment 2 so that the effect of the ambient wind on the nocturnal drainage flows is removed. No vegetation (bare soil) is used throughout the domain in experiment 3, and the distribution of vegetation in experiment 4 (not shown) is similar to the actual vegetation coverage: bare soil in the center of the basin and along the upper slopes of the sidewalls. Experiments 3 and 4 are performed because W96 speculated that vegetation may affect the downward turbulent heat flux. Tethersonde and airsonde observations revealed that wind directions and speeds varied significantly with time above the basin rim; therefore, experiments 5, 6, and 7 are performed with different initial wind directions up to 3.3 km above the basin floor to examine the effects of ambient wind direction on the cooling within the basin.

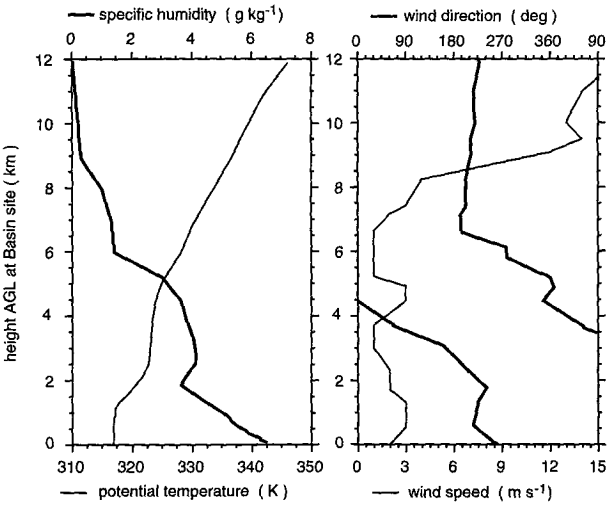

FIG. 2. Initial vertical profile of potential temperature, specific humidity, wind speed, and wind direction employed by experiment 1.

4. Numerical results

A comparison of the results from experiments 1 and 2 with the tethersonde measurements is made first to demonstrate that the model reproduces key features of the observed temperature and wind profiles during the experimental period. These key features include the amount of cooling in the center of the basin, light and variable winds at the basin site, and strong winds at the Salt Wash site. Then the predicted evolution of the slope flows, thermal structure, and heat budget within the basin are examined to identify mechanisms that lead to the strong cooling within the basin.

a. Comparison with observed profiles

Figure 3 depicts the predicted potential temperature profiles at the basin site for experiments 1 and 2 along with the tethersonde measurements. The predicted temperature profile gradually cools with time throughout the depth of the basin, although the cooling rate slows after 0100 MST. The final temperature profile at 0500 MST is nearly identical to the observed profile, indicating that the model correctly simulates the total amount of cooling in the basin during the evening. The observed temperature profiles, however, have stronger gradients within 100 m of the ground. This may be caused by insufficient vertical resolution or excessive vertical mixing near the surface. Experiment 1 also produces temperature profiles that are 2–5 K colder than observed above 200 m AGL between 2000 and 0100 MST. Although this also appears to be due to vertical mixing, it is mostly the result of cold air advection from the basin sidewalls, as will be shown in the next section. Experiment 2 (without ambient winds) produces temperature profiles with stronger vertical gradients near the surface in the early evening hours (1900–2100

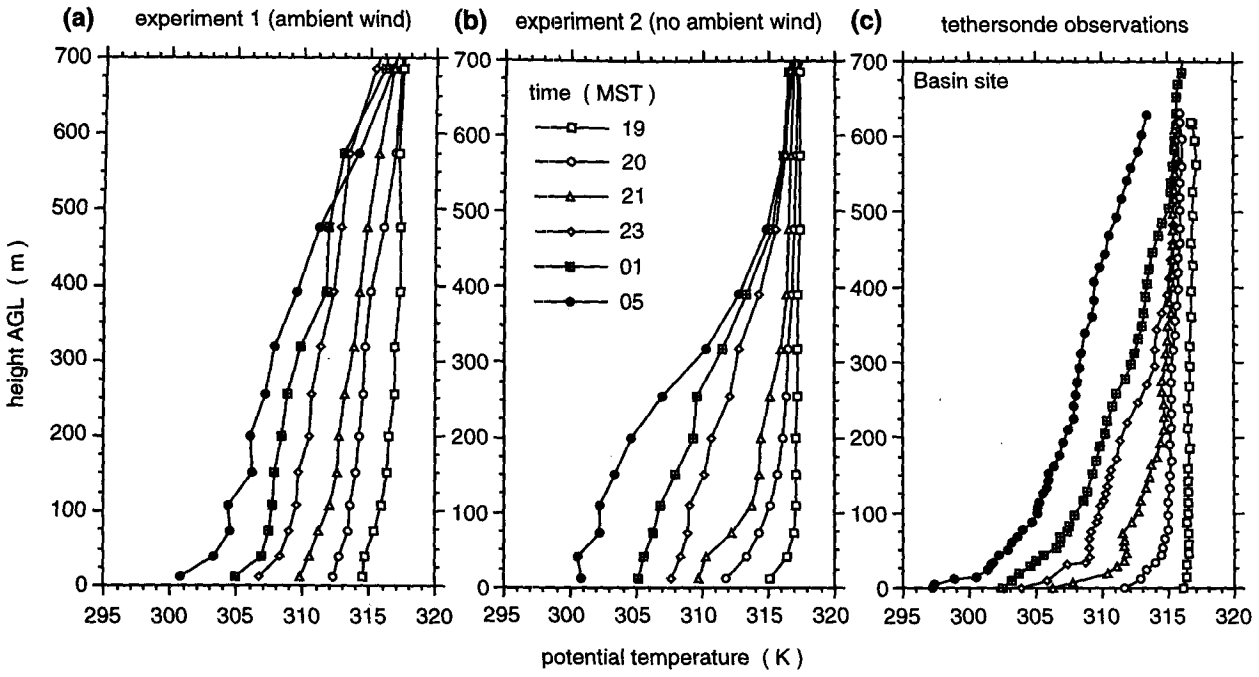

FIG. 3. Vertical profiles of potential temperature at the basin site predicted by experiments 1 and 2 and observations from the tethersonde.

MST) when compared to experiment 1. Nevertheless, the temperatures above 400 m AGL do not decrease significantly so that all of the cooling occurs in the lower part of the basin; the temperatures aloft are too warm and the temperatures near the surface are too cool by 0500 MST.

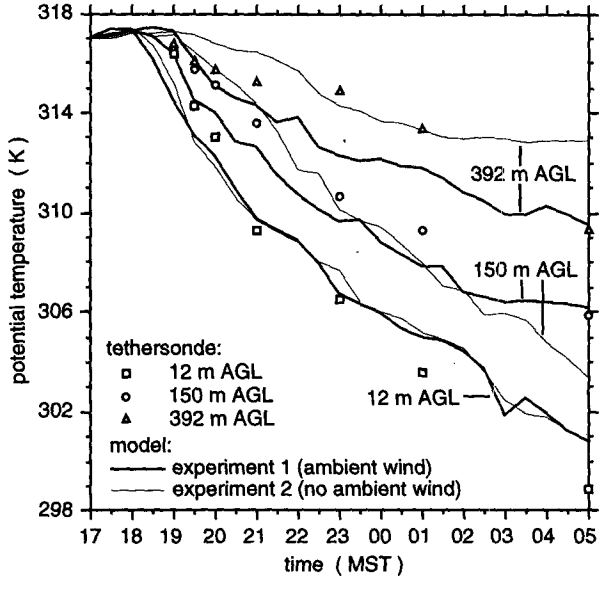

FIG. 4. Potential temperature predicted by experiments 1 and 2 at three selected heights along with observed values at the basin site.

To examine the nocturnal cooling at the basin site in more detail, the potential temperatures at three levels are shown in Fig. 4. Experiments 1 and 2 produce nearly the same temperature near the surface throughout the evening, indicating that the thermal forcing from the ground at the basin site is not affected by the ambient winds. Both simulations produce temperatures that are usually within 1.5 K of the observations, but the 392-m level temperatures from experiment 1 are 2–2.5 K too low at 2300 and 0100 MST, and the 150- and 392-m level temperatures from experiment 2 are as much as 3.5 K too high at 0500 MST. Some horizontal variation in potential temperature is produced by the model within 1 km of the basin site. The horizontal temperature differences are as much as 2 K at 2300 MST within a layer between 200 and 400 m AGL. Other potential temperature profiles within 1 km of the basin site are sometimes in better agreement with the tethersonde values.

The potential temperature profiles within the canyon at the Salt Wash site predicted by experiment 1 are similar to tethersonde observations (not shown); the model also produces the transient neutral layers near the lower parts of the canyon described by W96. These neutral layers are due to strong winds and wind shears within the canyon predicted by the model. The temperature profiles from experiment 2 did not contain neutral layers.

Figure 5 depicts the predicted wind speed profile at the Salt Wash site for experiments 1 and 2 along with the tethersonde measurements. Experiment 1 produces

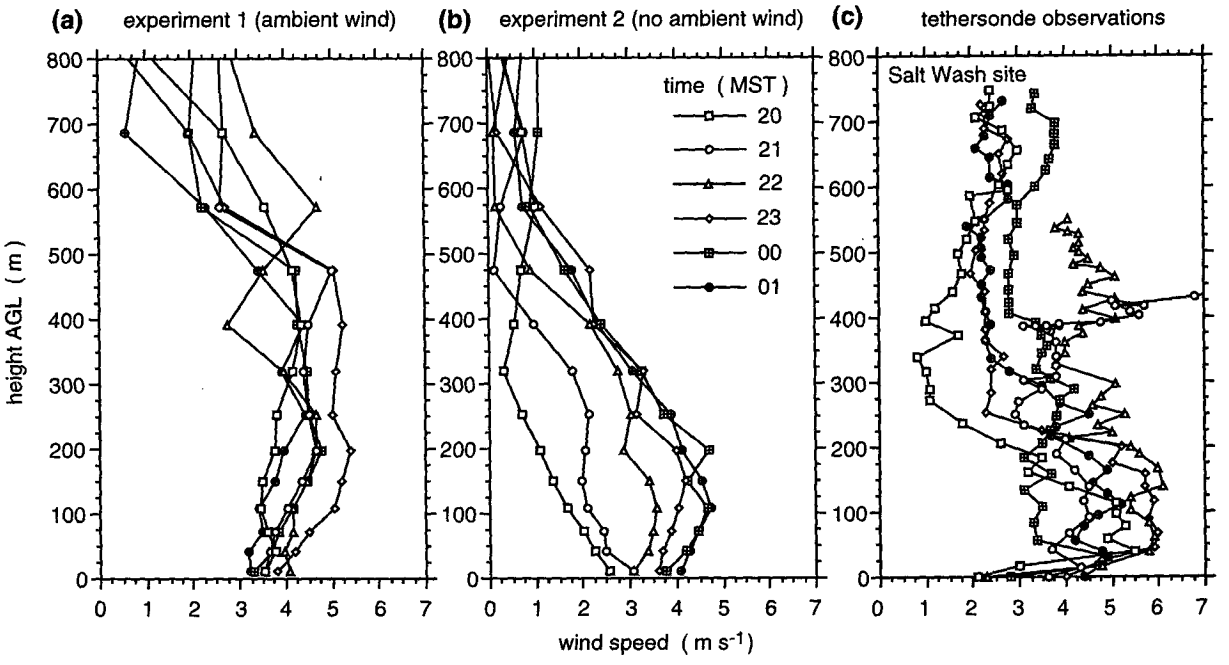

FIG. 5. Vertical profiles of wind speed at the Salt Wash site predicted by experiments 1 and 2 and observations from the tethersonde.

relatively strong winds exiting Sinbad Basin through the canyon with wind speeds of 4–5.5 m s^{-1} between 2100 and 0100 MST. This agrees with the observed profiles, although the observed maximum wind speeds are 0.5–1 m s^{-1} stronger. The weaker winds predicted by the model may be due to the differences between the modeled and observed temperature profiles within the basin as well as the representation of the canyon topography by the model (section 2a). The predicted wind speeds also vary within the canyon. For instance, the maximum wind speed 1 km further down the canyon and at 200 m AGL is 7.2 m s^{-1} at 2300 MST. Experiment 2 also produces strong winds within 200 m of the ground after 2200 MST, but the winds aloft are significantly weaker than those in experiment 1 and the observed profiles since all of the cooling within the basin occurs near the surface (Fig. 3b) in this simulation.

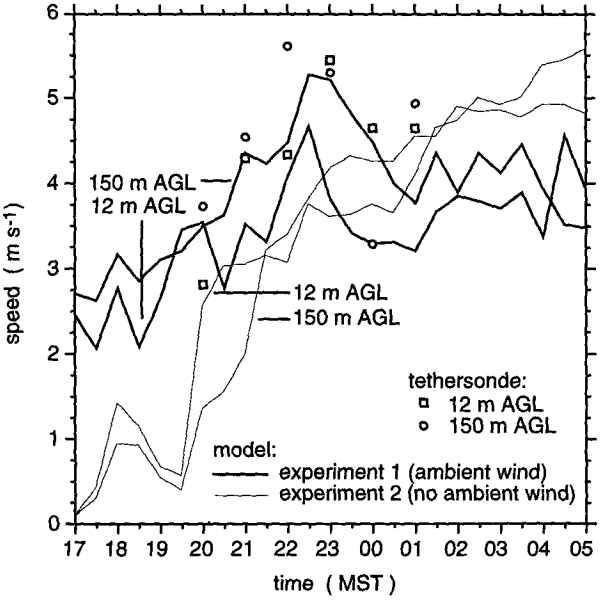

FIG. 6. Wind speed predicted by experiments 1 and 2 at two selected levels along with the observed values at the Salt Wash site.

Although the observed wind speed profiles at the Salt Wash site are quite complicated, the wind speeds within 200 m of the ground tend to increase until 2300 MST and decrease after this time. As shown in Fig. 6, this feature is produced only by experiment 1; experiment 2 produces wind speeds that increase with time during the whole evening. The peak wind speed in experiment 1 corresponds to the largest mass flux through the canyon and the largest pressure gradient computed between the Salt Wash site and the middle of the basin at a constant elevation of 2286 m MSL (not shown). Both the predicted pressure gradient and wind speed decrease until 0100 MST and remain nearly constant for the rest of the evening. At an elevation of 2286 m MSL, the potential temperature difference between the basin and the canyon increases from 0 to 2.5 K between 2000 and 2300 MST and then gradually decreases to 1.5 K by 0500 MST. These temperature differences produce a thermally developed pressure gradient that

drives the flow through the canyon. W96 found that the temperature difference computed from the tethersondes at 2214 m MSL was about 1.2 K at midnight. It is unclear why the model produces lower wind speeds with a larger temperature difference, but the model canyon geometry is probably one reason.

To obtain a quantitative measure of the model performance, the root-mean-square errors of potential temperature and wind speed, and the vector wind difference (VWD), are calculated at the tethersonde locations for experiments 1 and 2 and are given in Table 2. Both speed and direction errors are taken into account by the VWD that is given by

$$\mathrm{VWD} = [(u_m - u_0)^2 + (v_m - v_0)^2]^{0.5}, \quad (1)$$

where u_m, v_m and u_0, v_0 are the model and observed horizontal wind components. Even though the evolution of the stable boundary layer (Fig. 3) for experiments 1 and 2 is significantly different, the mean potential temperature errors during the evening are nearly identical. The root-mean-square error for wind speed and the VWD for these two experiments are about the same at the basin site, but the errors are smaller at the Salt Wash site for experiment 1 when ambient winds are included by the model.

As shown in W96, the winds in the middle of the Sinbad Basin atmosphere were light and variable for the evening of 15–16 July. This feature is reproduced well by both experiments 1 and 2 near the surface. The light and variable winds observed by the tethersonde imply that eddies may form within the basin, as will be shown in the following section.

TABLE 2. Summary of the root-mean-square errors for potential temperature (rms θ) and wind speed (rms s) and the vector wind difference (VWD) of the model calculated at the tethersonde observation locations.

	Experiment 1			Experiment 2		
Time (MST)	rms θ (K)	rms s (m s^{-1})	VWD (m s^{-1})	rms θ (K)	rms s (m s^{-1})	VWD (m s^{-1})
			Basin site			
1900	0.8	0.8	2.8	0.6	2.4	3.2
2000	0.9	1.9	3.1	1.0	1.8	2.6
2100	1.1	1.5	2.6	1.1	1.2	2.3
2300	1.6	1.3	1.5	0.8	0.8	1.1
0100	1.8	1.1	1.2	1.0	1.0	1.1
0500	1.1	0.9	1.8	2.7	0.5	1.6
Mean	1.2	1.2	2.2	1.2	1.3	2.0
			Salt Wash site			
1900	1.2	1.9	3.5	0.6	1.8	2.2
2000	1.2	1.0	1.7	0.8	2.7	2.9
2100	0.8	1.0	1.5	1.0	2.8	3.4
2300	1.5	1.6	2.0	0.8	1.3	2.2
0100	1.3	1.2	1.8	0.7	1.4	2.4
0500	1.4	1.2	1.7	1.0	0.9	2.2
Mean	1.2	1.3	2.0	0.8	1.8	2.5

b. *Basin circulations*

The u component of the wind from experiment 1 on vertical cross section AA' (Fig. 1) is shown in Fig. 7 for three times during the evening. At 2100 MST, strong downslope flows up to 5.6 m s^{-1} are evident on the western slope and weaker downslope flows up to -1.9 m s^{-1} occur on the eastern slope. The magnitude of the downslope flow is also stronger on the western slope of the basin in experiment 2, although the difference is not as great. For example, the maximum u component at 2300 MST is 3.3 and -2.4 m s^{-1} on the western and eastern slopes, respectively (not shown). Since there are no ambient winds in experiment 2, the stronger drainage winds over the western slopes are probably due to the relatively large area surrounding Pace Peak that is a source of cold air draining into the basin. The eastern ridge of the basin (Sewemup Mesa) is relatively narrow so that drainage flows developing on this slope are due almost entirely to local cooling. This suggests that the asymmetry of the u component in experiment 1 occurs because the ambient winds enhance the drainage flows over the western slope, while retarding their development on the eastern slope. This effect is similar to the numerical results presented by Doran (1991) in which the ambient wind crossed an idealized symmetrical valley.

Cold air flows into the basin the entire evening, but a significant portion of the drainage flow becomes elevated by 2300 MST, as seen in Fig. 7b. A shallow layer of drainage winds still follows the terrain to the middle of the basin floor at this time. By 0100 MST, the intensity of the surface drainage winds decreases and most of the air that enters the basin becomes detached from the sidewalls. A significant portion of the drainage winds in experiment 2 also becomes elevated above the surface after 2300 MST, although the magnitude of the wind speeds along cross section AA' is usually less than 2 m s^{-1}. Also shown in Fig. 7 is the vertical cross section of the particle plume released from the western sidewall site (Fig. 1b). The particle plume initially remains near the surface, but it splits as the drainage flow becomes elevated after 2300 MST. While the maximum particle concentration is at the same level as the cross-basin maximum wind speed, a portion of the plume continues to follow the terrain to the bottom of the basin during the whole simulation.

The model predicts a complex wind field on the basin floor by 2100 MST, as seen in Fig. 8. Drainage winds of 2–4 m s^{-1} follow the local slopes from Pace Peak down into the western portion of the basin, and strong downslope winds up to 6 m s^{-1} occur on the west and southwest slopes of the basin at this time. The winds over the mesa top on the eastern side of the basin are also southwesterly, but later in the evening these areas

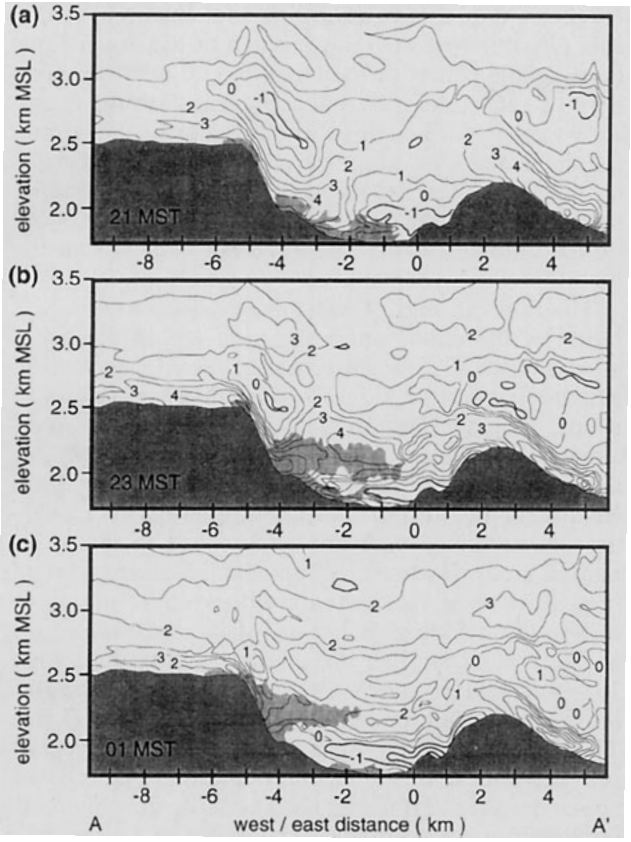

FIG. 7. Vertical cross section along AA' (Fig. 1b) of the predicted u component (contour interval 1 m s^{-1}) and tracer concentration greater than 0 (shaded) at (a) 2100, (b) 2300, and (c) 0100 MST from experiment 1.

also drain into the basin (not shown). The structure of the drainage winds along the northwestern sidewalls appears to be affected by the small-scale valleys and ridges that run perpendicular to the basin rim. Maximum wind speeds of just over 4 m s^{-1} occur inside two of these small-scale valleys, while weaker winds occur along the ridges perpendicular to the basin rim. The wind directions and areas of maximum wind speeds from experiment 2 at this time are very similar to those shown in Fig. 8, except that the wind speeds are weaker (the maximum wind speeds over the northwestern and southwestern sidewalls are 3.6 and 2.6 m s^{-1}, respectively) and the drainage winds flow into the basin along the eastern sidewalls. This indicates that the northern slopes of the basin are largely unaffected by the ambient winds. The ambient winds increase the magnitude of the downslope flows along the southwestern sidewalls and divert part of the drainage flow within the narrow valley just south of Sinbad Ridge into the basin.

Despite the strong downslope winds on the west and southwest slopes, the flows on the basin floor appear to be affected primarily by the drainage winds from the northern part of the basin. The drainage winds from the northwestern sidewall flow south to form a counterclockwise eddy in the middle of the southern basin floor as shown in Fig. 8a. The eddy actually persists through much of the evening until 0400 MST, but the center moves back and forth across the southern portion of the basin. Other eddies form near the surface on the basin floor and along the sidewalls during the evening, but they are smaller and more transient. Petkovsek (1978) employed an analytical technique and observations in Slovenia to demonstrate that drainage flows within a closed basin can converge closer to the steepest sidewall. He found that downslope flows over a steep slope may not penetrate far into the basin as a result of intense adiabatic warming that decelerates the drainage winds. In the Sinbad Basin, relatively steep slopes

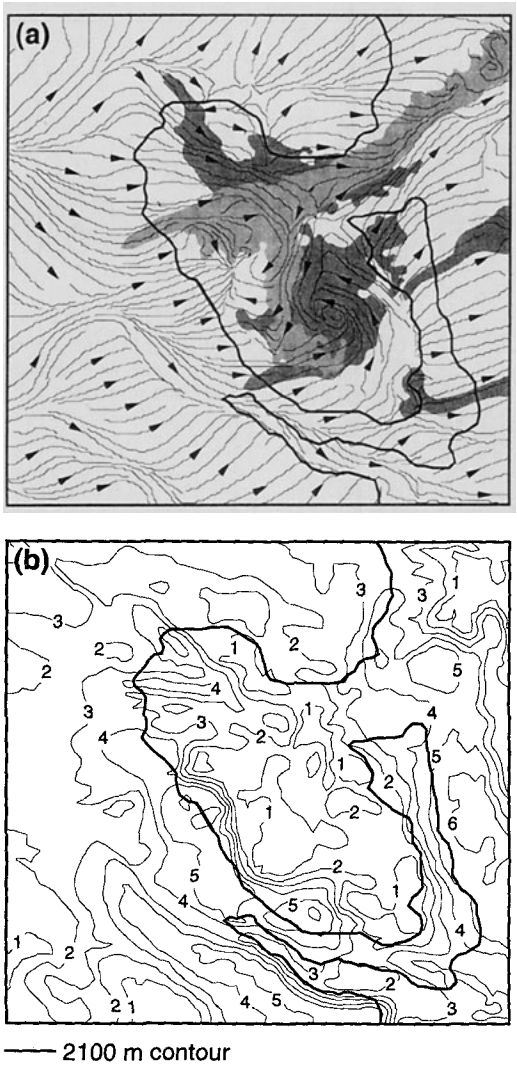

FIG. 8. Near-surface wind field at 12.5 m AGL predicted by experiment 1 at 2100 MST: (a) streamlines and isosurface of three-dimensional tracer plumes projected onto the ground (shaded) and (b) wind speed (contours of 1 m s^{-1}).

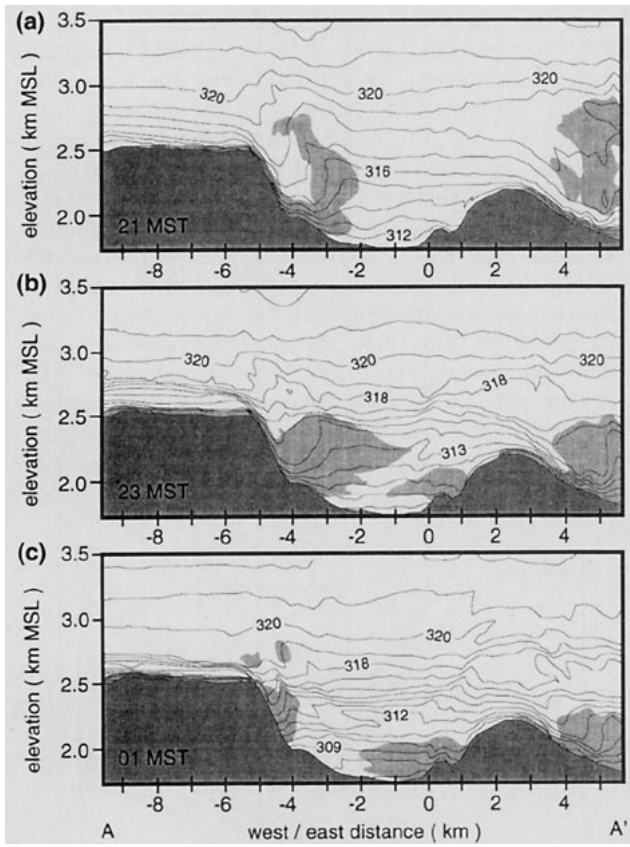

FIG. 9. Vertical cross section along *AA'* (Fig. 1b) of the predicted potential temperature (contour interval 1 K) and TKE greater than 0.2 m^2 s^{-2} (shaded) at (a) 2100, (b) 2300, and (c) 0100 MST from experiment 1.

surround the relatively flat southern basin floor, whereas the northern basin floor has gradual slopes (Fig. 1b); therefore, the mechanism proposed by Petkovsek (1978) may explain the near-surface convergence in the southern basin that persists for most of the evening.

Most of the particle plume released from the western sidewall site advects directly through the basin into the canyon, but the shallow northerly flow along the basin floor also transports part of the plume into the eddy at 2100 MST (Fig. 8a). Particles released from the southwestern sidewall site are advected into and recirculated within the eddy before they are advected out of the basin through the canyon 1 hour later. The plumes from the southern and eastern sidewalls are largely advected by the ambient winds at this time, but they do drain into the basin by 2300 MST. By 0200 MST, particles released from the northern sidewall are found over much of the basin floor, but they are retarded by drainage flows coming down the eastern sidewalls. By the end of the evening, particles fill up the basin volume below the height of the eastern basin rim (not shown). While it is possible that the convergence of the downslope flows in the center of the basin would result in positive vertical velocities that could transport the tracer above the basin lid, this did not occur in this simulation. Instead the majority of the particles exit the basin through the Salt Wash Canyon, while some of the particles at the top of the cloud are sheared off by the ambient winds and advected over the mesas on either side of the canyon.

The flows in Figs. 7 and 8 are coupled to the evolution of the temperature structure within the basin as shown in Fig. 9. Early in the evening, cold air generated over the slopes of Pace Peak is advected by the drainage and ambient winds down the steep slopes of the basin, resulting in a hydraulic jump on the western side of the basin by 2100 MST (Fig. 9a). Relatively high turbulence kinetic energy (TKE) values are produced near the surface and in the near-neutral areas. Hydraulic jumps that result from stratified flow over escarpments with slopes similar to those within Sinbad Basin have also been observed and simulated by other investigators (Pitts and Lyons 1989; Blockley and Lyons 1994). The hydraulic jump diminishes in magnitude by 2300 MST, but TKE generated along the sidewalls is now advected into the middle of the basin. While the whole basin cools between 2100 and 2300 MST, the potential temperature gradient throughout the basin remains nearly the same. The cooling aloft is due predominantly to the advection of cold air from the sidewalls (Fig. 7b), but there is sufficiently high TKE to also

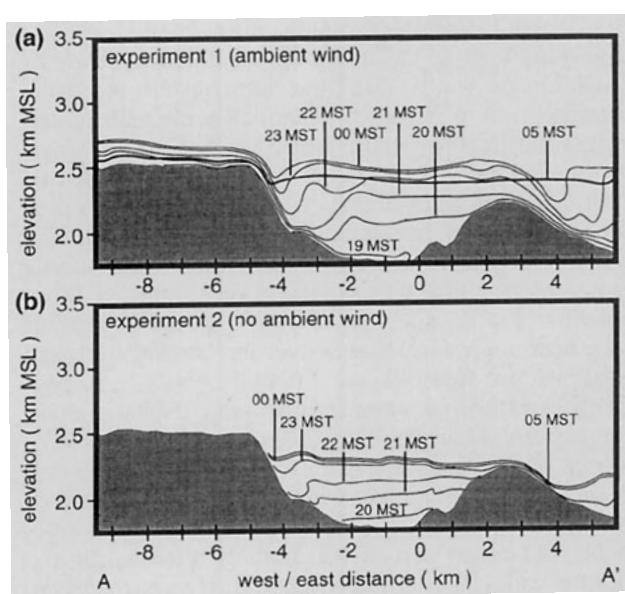

FIG. 10. Position of 315-K isotherm along vertical cross section *AA'* (Fig. 1b) as a function of time for (a) experiment 1 and (b) experiment 2.

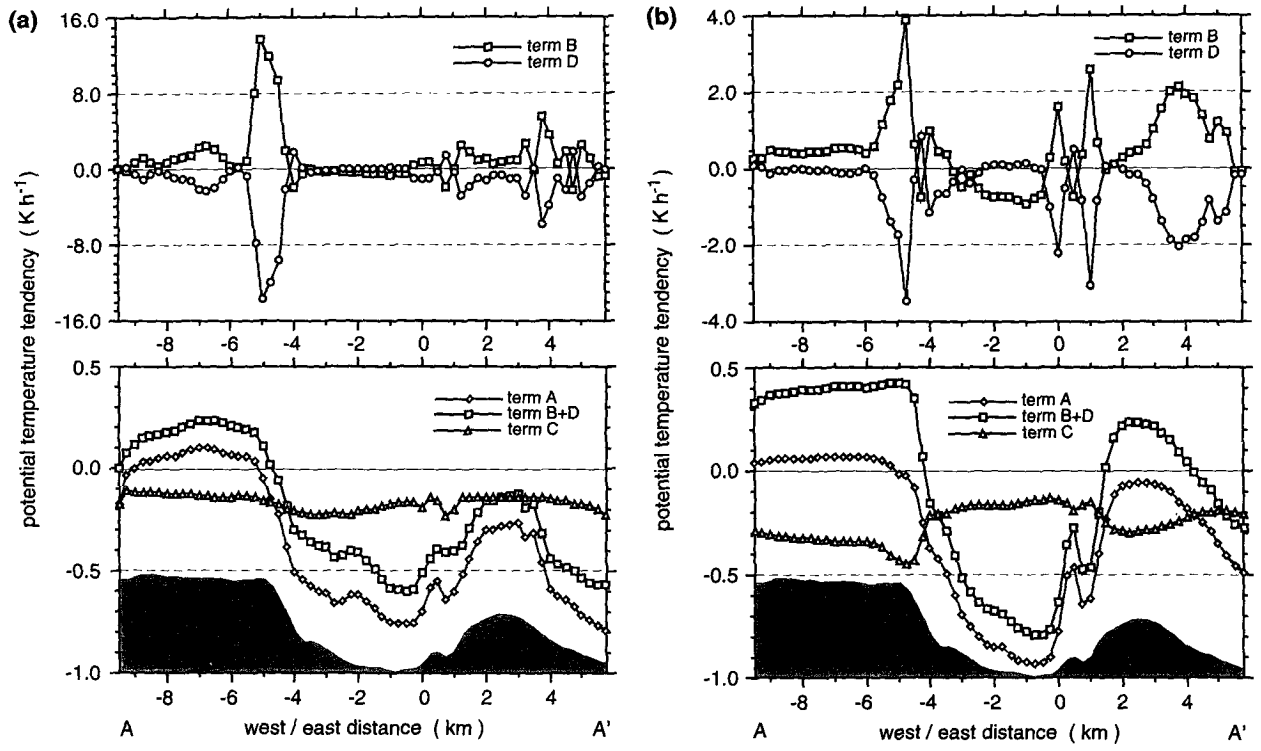

FIG. 11. Individual terms of the potential temperature tendency equation, Eq. (2) (averaged between 2000 and 0500 MST and normalized by h), along cross section AA' for (a) experiment 1 and (b) experiment 2.

mix cooler temperatures upward. A strong temperature gradient cap develops just above the basin lid by 2300 MST since the temperatures above the basin lid remain relatively constant. By 0100 MST, the vertical potential temperature gradient within the basin increases and the amount of TKE advecting into the center of the basin decreases. The drainage flows become partially elevated after 2300 MST (Fig. 7b) because they are relatively warmer than the cold air adjacent to the basin floor. As the evening progresses, the drainage flows weaken and do not penetrate as deeply into the basin.

The evolution of the thermal structure is given in Fig. 10 by plotting the position of the 315-K isotherm through the basin cross section as a function of time for experiments 1 and 2. In experiment 2, the isotherm gradually rises with time until it reaches a steady-state height above the basin lid by 2300 MST. Since the height of the 315-K isotherm remains steady while the basin continues to cool, the gradient increases within the basin after 2300 MST. The potential temperature evolution is nearly uniform in experiment 2, although there is a tendency for slightly lower temperatures on the eastern side of the basin. In experiment 1, spatial inhomogeneity in the cooling is clearly evident. The hydraulic jump between 2000 and 2300 MST produces downward vertical advection of warmer potential temperatures over the western side of the basin with upward vertical advection of cooler air above the middle western slopes. By 0000 MST the maximum height of the 315-K isotherm is reached, but it slowly sinks 100 m by the morning.

Even though the cooling rate in the model at the basin site differs from the tethersonde observations in some respects, experiment 1 reproduces the temperature profile at 0500 MST quite well, suggesting that the net cooling within the basin during the evening is reasonably simulated. Therefore, the model results can be analyzed further to provide information regarding the role of slope flows on the basin heat budget.

c. *Basin heat budget*

One of the advantages of applying a mesoscale model to simulate the flows in the Sinbad Basin is that the model produces a thermodynamically balanced dataset that can be used to examine the individual terms of the atmospheric heat budget (Zhong and Whiteman 1995). The relative importance of each of these terms was determined for all the simulations in Table 1, although most of the discussion here will focus on experiments 1 and 2. The terms of the heat budget are

calculated by vertically integrating the thermodynamic equation to obtain

$$\underbrace{\int_{z_g}^{h} \frac{\partial \theta}{\partial t}\, dz}_{\text{A}} = \underbrace{\int_{z_g}^{h} -\nabla\cdot(\mathbf{V}\theta)\, dz}_{\text{B}} + \underbrace{\int_{z_g}^{h} -\frac{\theta}{T\rho c_p}(\nabla\cdot(\mathbf{R})\, dz}_{\text{C}} + \underbrace{\int_{z_g}^{h} \frac{\partial}{\partial z} K_H \frac{\partial \theta}{\partial z}\, dz}_{\text{D}} \quad (\text{K m s}^{-1}), \quad (2)$$

where the local rate of change of potential temperature in a vertical column (A) results from an imbalance between advection (B), radiative flux (C), and turbulent diffusion (D). Equation (2) is integrated from the surface z_g to a height h, approximately 800 m AGL. This level was chosen because it is somewhat above the basin lid where the contributions to Eq. (2) become small. The terms in Eq. (2) from experiments 1 and 2, averaged between 2000 and 0500 MST and normalized by h, are shown in Fig. 11 as a function of location along basin cross section AA'. A 9-h average is taken to depict the cooling mechanisms within the basin during the entire evening.

In experiment 1, advection and turbulent diffusion are the dominant terms in Eq. (2) along the sidewalls, with the largest values over the western slope (Fig. 11a). West of the basin, these two terms contribute to a net warming in the layer as warmer potential temperatures are advected from the slopes surrounding Pace Peak. Cooling due to turbulent diffusion is greater than advective warming over the upper half of the western sidewall and over most of the eastern sidewall during the evening. Along the lower western sidewall slopes and in the middle of the basin, turbulent diffusion becomes nearly zero so that the cooling is due to local radiative cooling and the advection of cold air from the sidewalls. The measurements made by W96 also showed virtually no turbulent sensible heat flux on the basin floor. Interestingly, the magnitude of the average local change in potential temperature (term A) given by Eq. (2) nearly parallels the underlying terrain elevation, with the strongest cooling in the center of the basin. This happens because the lowest elevation in the center of the basin is where the coldest air accumulates, producing the greatest heat loss during the evening. Since the other terms in Eq. (2) are not uniform across the basin, the largest value of term A, -1.17 K h^{-1}, occurs at the base of the southern sidewall. The correlation coefficient of term A and the terrain elevation is 0.66, based on the values from all of the grid points below 2200 m MSL.

Advection and turbulent diffusion are also the dominant terms in Eq. (2) for experiment 2 (Fig. 11b); however, their magnitude is smaller than in experiment 1 because of the weaker slope flows. Since the drainage flows from experiment 2 are the strongest over the western basin slopes, these two terms are also the largest over the western slope. The storage term closely follows the underlying terrain as in experiment 1, but the correlation coefficient of term A and the terrain elevation is now 0.99. The greatest heat loss in experiment 2 occurs in the center of the basin; therefore, the magnitude of term A in Fig. 11b is slightly larger than in Fig. 11a.

Even though the average cooling depicted in Figs. 11a and 11b during the evening is rather simple, the

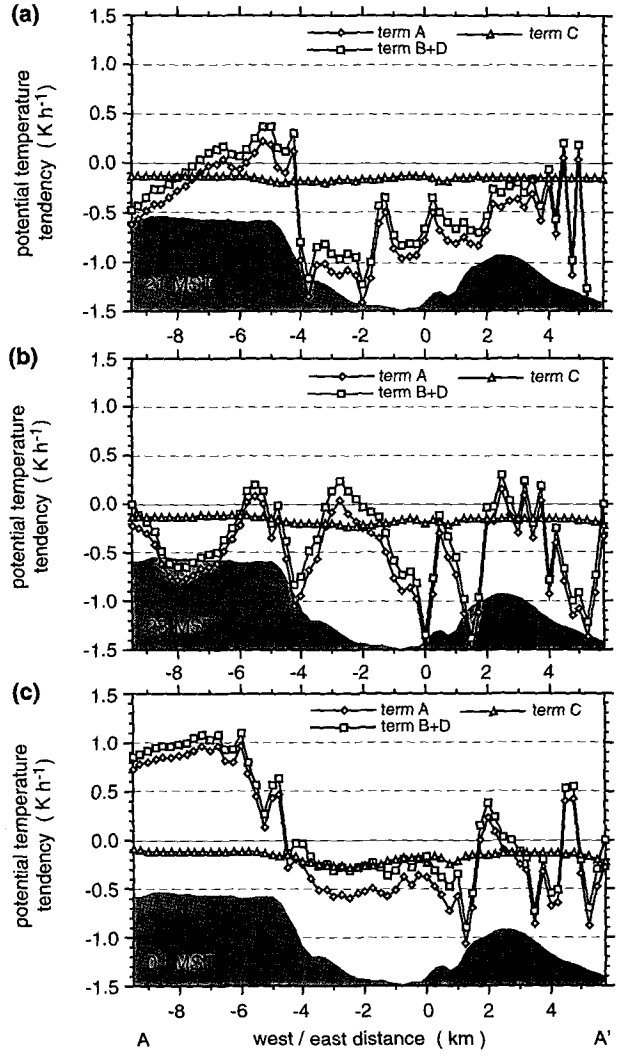

FIG. 12. Individual terms of the potential temperature tendency equation, Eq. (2) (averaged over 30-min intervals and normalized by h), along cross section AA' for experiment 1 at (a) 2100, (b) 2300, and (c) 0100 MST.

rate of cooling within the basin varies significantly in space and time. For example, the terms in Eq. (2) from experiment 1, averaged over 30-min intervals and normalized by h, are shown in Fig. 12 at three times during the evening. The radiation flux divergence does not vary significantly in space or time so that the complicated local rate of change of potential temperature at any one time is due to subtle differences between the advection and turbulent diffusion terms. The complex circulations within the basin (Fig. 8) no doubt contribute to the variation of the terms in Eq. (2) across the basin floor. In general, relatively strong cooling rates along the sidewalls result from large turbulent diffusion values, while strong cooling rates in the middle of the basin are usually due to advection of cold air from the sidewalls. Vertical advection is another mechanism that cools the basin atmosphere at certain times during the simulation period; low potential temperatures at the surface are advected upward by both strong upward vertical velocities within the hydraulic jump along the lower slopes of the western sidewall (Fig. 9a) and modest upward vertical velocities associated with the converging downslope flows early in the evening (Fig. 7a). There are also mechanisms that occasionally result in warming within the basin. For instance, horizontal advection of a layer of higher potential temperatures by the elevated drainage flow (Fig. 7b) warms the center of the basin at 2300 MST (Fig. 9b). Radiative flux divergence and advection of cold air from the sidewalls contribute equally to cooling in the center of the basin after 0100 MST (Fig. 12c).

Integrating the thermodynamic equation over the volume of the basin results in the atmospheric heat budget equation given by

$$\underbrace{\iiint \rho c_p \frac{\partial \theta}{\partial t}\, dV}_{\text{A}} = \underbrace{\iiint -\rho c_p \nabla\cdot(\mathbf{V}\theta)\, dV}_{\text{B}} + \underbrace{\iiint -\frac{\theta}{T}(\nabla\cdot\mathbf{R})\, dV}_{\text{C}} + \underbrace{\iiint \rho c_p \frac{\theta}{\partial z} K_H \frac{\partial \theta}{\partial z}\, dV}_{\text{D}} \quad \text{(W)}, \quad (3)$$

which specifies that the change in heat storage (A) results from an imbalance between the convergence of potential temperature flux by the mean wind (B), the convergence of radiative flux (C), and the convergence of the turbulent sensible heat flux (D) in the atmospheric volume. These terms are calculated from the model results using all the grid points below the 2200-m contour (Fig. 1b) and west of an arbitrary line across the canyon about 1 km west of the Salt Wash site. Before the values are integrated in Eq. (3), the model results are interpolated to another vertical grid that employs a 40-m grid spacing up to the basin lid height that is defined here at 2200 m MSL (approximately the same height used by W96).

The variation of the atmospheric heat budget terms with time, given by Eq. (3) and normalized by the basin area, for experiments 1 and 2 is shown in Fig. 13. Cooling is due to radiative and turbulent sensible heat flux during the evening, while advection warms the basin. Radiative flux divergence is nearly constant, at 35 W m^{-2}, but the magnitude increases slightly with time during the evening. Both experiments suggest that the strongest cooling within the entire basin occurs in the early evening between 1900 and 2300 MST. In experiment 1, advective warming increases slowly with time, while the turbulent sensible heat flux term remains relatively constant after 2300 MST so that the rate of heat storage loss from the basin decreases later in the evening (Fig. 13a). The rate of the heat storage loss from experiment 2 also decreases after 2300 MST, but in this case it results from advective warming increasing faster than turbulent sensible heat flux cooling as the evening progresses (Fig. 13b). While the results from experiments 1 and 2 are similar, the ambient winds had a significant impact on the heat budget within the basin. Table 3 gives the values of the terms in Eq. (3) averaged between 2000 and 0500 MST and indicate that

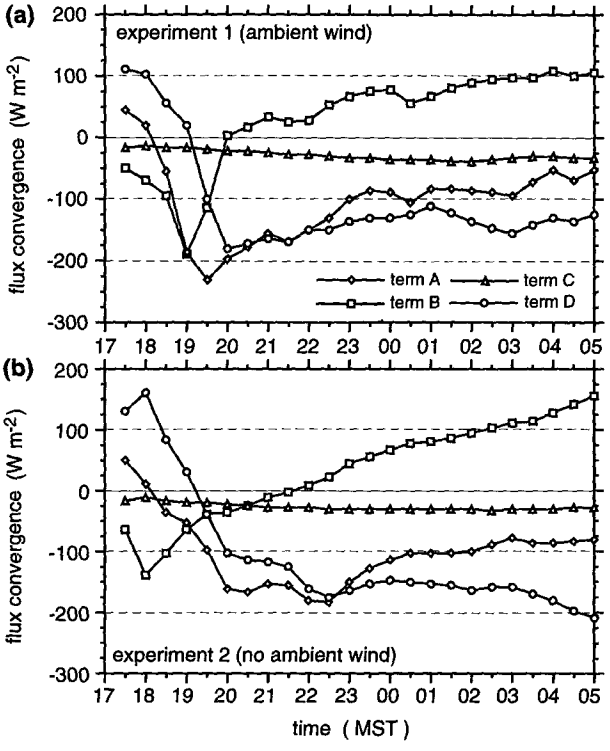

FIG. 13. Individual terms of the heat budget equation, Eq. (3) (normalized by the basin area), as a function of time for (a) experiment 1 and (b) experiment 2.

TABLE 3. Summary of the heat budget terms (W m^{-2}) within the basin averaged between 2000 and 0500 MST.

Experiment	Storage (term A)	Horizontal advection	Vertical advection	Advection (term B)	Radiative flux (term C)	Turbulent diffusion (term D)
1	−108.0	−348.5	416.1	67.6	−32.4	−143.2
2	−120.8	−93.4	158.1	64.7	−29.3	−156.2
3	−124.6	−263.8	336.4	72.6	−50.5	−146.7
4	−116.0	−314.2	383.3	69.1	−43.7	−141.4
5	−89.9	−292.6	376.4	83.8	−34.4	−139.3
6	−140.2	−184.4	162.5	−21.9	−41.3	−77.0
7	−149.2	−183.1	141.1	−42.0	−36.6	−70.6

the ambient winds reduced the overall cooling of the basin when compared to experiment 2.

To illustrate the possible effect of vegetation on the cooling rate within the basin, the variation of the normalized atmospheric heat budget terms with time from experiments 3 and 4 is shown in Fig. 14. In experiment 3 (Fig. 14a), a uniform bare soil surface leads to a radiative flux divergence that is 1.5–2 times larger than the radiative flux divergence from experiment 1 during most of the evening. When the model incorporates a heterogeneous vegetation distribution (Fig. 14b), the atmospheric heat budget terms are similar to those from experiment 1. The bare-soil areas on the basin floor in experiment 4 increase the radiative flux divergence somewhat and decrease the contribution from the turbulent sensible heat flux, leading to cooling within the basin that is slightly higher than for experiment 1 (Table 3). In contrast to experiments 1 and 3, the radiative flux divergence from experiment 4 can vary by a factor of 2 across the basin (not shown).

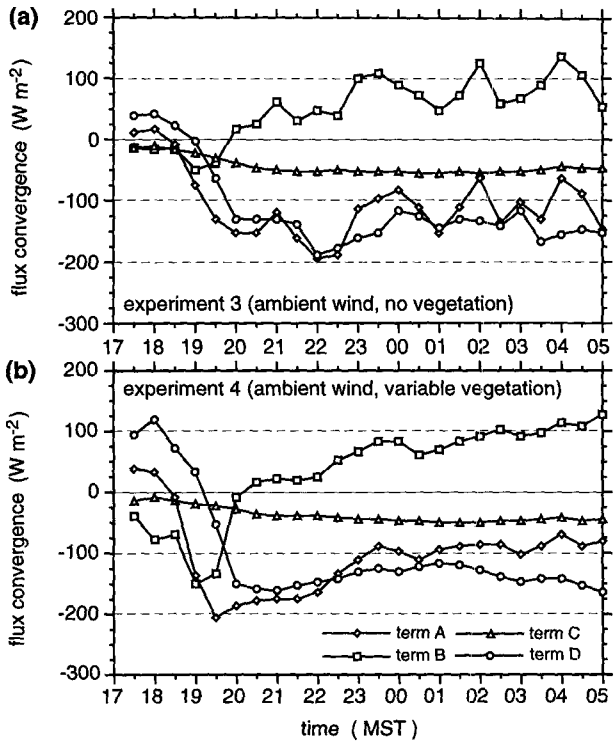

FIG. 14. Same as Fig. 13 except for (a) experiment 3 and (b) experiment 4.

The direction of the ambient winds also modifies the heat storage within the basin, as seen in Table 3. The ambient northwest winds in experiment 5 produce less horizontal advection so that the basin becomes somewhat warmer than in experiment 1. This implies that the local topography will have an impact on the drainage flows that will ultimately affect the amount of cooling. When the ambient winds have an easterly component, as in experiments 6 and 7, very strong cooling occurs within the basin. In these simulations, the surface temperatures at the basin site are similar to those from experiment 1 (Fig. 4), but the potential temperature profiles are nearly neutral and the temperatures aloft are much lower than those shown in Fig. 3a. The lower potential temperatures aloft result from the relatively low magnitude of the vertical advection term. When the winds are from the west, the hydraulic jump on the steep slopes of the basin (Fig. 9) brings higher potential temperatures down from aloft resulting in a net warming of the basin atmosphere. This mechanism is not as effective when the winds are from the east since the eastern rim is lower in elevation and not as steep overall.

5. Discussion

Observations from the basin site tethersonde suggest that pooling of cold air in the basin results in a strong stable layer near the surface early in the evening that grows in depth through the night. Above the stable layer, a residual neutral layer exists that cools uniformly only by 1–2 K by 2300 MST. In experiment 1, the near-surface temperatures are well predicted, but the boundary between the surface stable layer and the residual layer within the basin is not as distinct as the observations because the model cools the basin atmosphere in this volume too quickly. While the temperature profiles aloft remain nearly neutral, the whole profile decreases by as much as 5 K by 2300 MST, producing relatively weak vertical gradients near the surface.

As stated previously, the weaker stable layer near the surface and the relatively strong rate of cooling in the middle of the basin atmosphere may be due to a vertical grid spacing that is not sufficient to resolve the shallow drainage flows along the slopes of the basin or to vertical mixing that is too strong in the middle basin atmosphere. Additional test simulations were performed to examine these possibilities.

Two two-dimensional simulations were performed using topography along basin cross section *AA'* to evaluate the effect of vertical grid spacing. The same grid spacing as in experiment 1 (section 2a) was used for one simulation, and twice the vertical resolution and a horizontal grid spacing of 150 m was used for the other simulation. Decreasing the vertical grid spacing also required that the horizontal grid spacing and the time step be reduced. The depth and evolution of the drainage flows along the basin sidewalls from both the high- and low-resolution simulations were qualitatively very similar. As in Fig. 7, a portion of the drainage flow became elevated in both simulations. Slightly stronger vertical potential temperature gradients were produced in the middle of the basin by the high-resolution simulation; however, these gradients were still not nearly as strong as those observed by the tethersonde. A three-dimensional simulation with a higher resolution than experiment 1 is computationally expensive and the two-dimensional tests indicate that increasing the spatial resolution may not significantly improve the model results. Conversely, two-dimensional tests cannot fully determine whether three-dimensional features, such as the canyon, need to be resolved with a smaller horizontal grid spacing.

Two additional three-dimensional simulations were performed to examine the effect of turbulent diffusion, term D in Eq. (2), on the model results. The simulations were identical to experiment 1, except that they employed different length-scale formulations that reduced the TKE and vertical eddy exchange coefficients in the middle basin atmosphere. The potential temperature profiles from these simulations were similar to those in Fig. 3a, indicating that excessive vertical mixing may not be responsible for the weak surface temperature gradients or the high rate of cooling in the middle basin atmosphere.

Evaluation of individual terms of the heat budget equation reveals that the simulated cooling aloft in the middle of the basin is due primarily to advection of cold air from the sidewalls rather than turbulent diffusion. The excessive cooling at these levels (Figs. 3a and 3c) thus suggests that the simulated elevated winds may be too strong. For instance, the model produces southwesterly wind speeds up to 4 m s^{-1} 400 m above the basin floor at 2300 MST (Fig. 7b) and the observed elevated maximum wind speed at the basin site is 2.8 m s^{-1}. The model wind speed decreases to 2.3 m s^{-1} by 0100 MST, but the observed elevated wind speed maximum is 1.5 m s^{-1} at that time. The observed wind speeds aloft at the basin site are more transient than those produced in experiment 1, and there are no other observations to confirm whether strong elevated wind speed maxima occur at other locations. Varying the ambient wind direction (experiments 5, 6, and 7) did affect the amount of cooling due to advection within the basin, and it is likely that the amount of cooling is also dependent upon the ambient wind speed. Higher ambient wind speeds would increase vertical motions over the sidewalls and enhance the entrainment of air aloft into the basin as described by Doran (1991). To further examine the effect of ambient wind direction and speed, an additional three-dimensional simulation was performed that employed four-dimensional data assimilation (Fast 1995) to incorporate the tethersonde winds above the basin rim elevation into experiment 1. As expected, the wind speed and direction errors at the basin and Salt Wash sites were reduced somewhat in this simulation. The amount of cooling due to advection near the basin rim elevation was smaller in the data assimilation experiment than in experiment 1; nevertheless, the potential temperature profiles were nearly identical to those in Fig. 3a and the heat budget was similar to Fig. 13a. Despite the fact that the rate of cooling in the model at the basin site differs from the tethersonde observations in some respects, the model reproduces the temperature profile at 0500 MST quite well, indicating that the net cooling within the basin during the evening is reasonably simulated.

One of the objectives of this study was to determine the effect of the sidewall drainage flows on the basin heat budget by comparing the terms in Eq. (3) produced by the model with those computed from the observations alone (W96). The relative contributions of the individual terms in Eq. (3) for both the model and the observational method are very similar when the results from experiment 1 (Fig. 13a) are compared with the values given by Fig. 11 of W96; however, the magnitudes are significantly different. Both the model and the observational method suggest that the magnitude of the heat storage change term is largest in the early evening around 2000 MST, but the model value is about 2.5 times larger than the value obtained using the observational method. The difference in the heat storage term gradually decreases to nearly zero by 0500 MST. At 0000 MST, the radiative flux divergence in the model is about 1.5 times larger than for the model employed by W96, while advection in the model is about 3.5 times larger than for the observational method. These differences may indeed suggest that it is important to account for the inhomogeneity in the flows within the basin (as shown in Figs. 7, 9, and 10) when computing the heat budget. Nevertheless, the flow fields along the sidewalls cannot be verified, so we can only speculate that the model is producing a reasonable estimate of their contribution to the basin heat budget.

The observational method in W96 assumes horizontal homogeneity of the meteorological fields based on

measurements from the basin site, but these measurements are clearly not representative of the entire basin. However, the model results from experiment 1 suggest that the assumptions employed by W96 for the vertical advection term may be reasonable; the mean vertical velocity on the 2200-m MSL surface is around 0.025 m s^{-1} (nearly identical to the values used by W96), and the simulated potential temperatures are nearly horizontally homogeneous within the basin after midnight.

The differences in the magnitude of the heat budget terms between the model and the observational method can also be attributed to model forecast errors since the model does not produce a perfect forecast of the observed temperature profiles within the basin. The largest differences in the heat storage change term occur early in the evening when the temperature errors at the basin site are also the largest.

The advantage of the model heat budget is that it includes contributions from the complex circulations within the basin. While additional observations at different locations within the basin would increase the confidence of the estimate of the observational heat budget, other studies have shown that a very dense observational network would be required in complex terrain to adequately resolve the spatial and temporal meteorological fields. For instance, the heat budget equation computed by Bader and Horst (1990, 1992) did not balance when observations from the relatively dense measurement network around the Brush Creek Valley (Clements et al. 1989; Horst et al. 1987) were used in their analysis.

W96 developed a convenient way of comparing the heat budget of multiple valleys and basins by nondimensionalizing Eq. (3) to obtain

$$\frac{A}{C+D} - \frac{B}{C+D} = 1. \qquad (4)$$

Equation (4) provides a basic measure of the relative contributions from heat storage or advection, and the results from the experiments in this study are shown in Fig. 15. Advection is larger than heat storage for values on the right side of the plot, corresponding to the heat budgets of valleys. Heat storage is larger than advection for values on the left side of the plot, corresponding to the heat budgets of closed basins (W96). The results from experiments 1, 2, 3, and 4 fall on the left side of the plot, indicating large amounts of heat loss associated with a basin, but advection is large enough to suggest that the basin is not completely closed. These results seem more reasonable than the value computed by W96 because of the relatively large mass flux through the canyon. The clustering of these points also indicates that vegetation did not significantly change the relative contributions of the advection and heat storage terms within the basin. The results from experiment 5, with northwest ambient winds, produce a larger advection term than the control simulation, suggesting

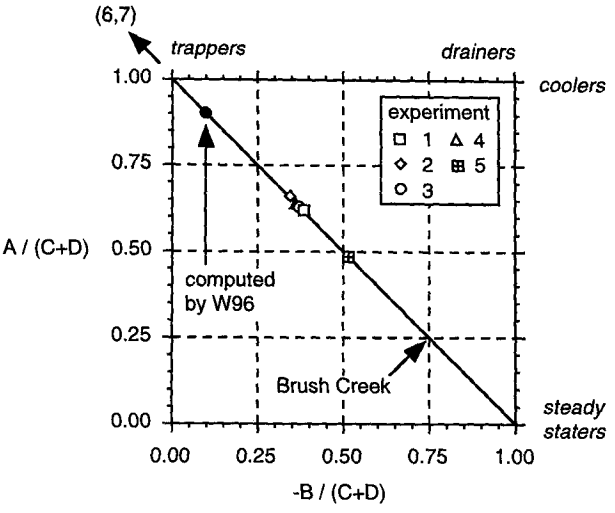

FIG. 15. Categorization of experiments with respect to the ratio of selected heat budget terms.

that the basin behaves more like a valley when the ambient wind enhances the flow through the Salt Wash Canyon. The two simulations that had easterly winds indicate that the basin is closed and traps the drainage flows. In fact, the northeast ambient winds in experiment 7 retarded the drainage winds within the Salt Wash Canyon during most of the evening.

6. Summary and conclusions

A mesoscale model has been used to simulate the evolution of the boundary layer within Colorado's Sinbad Basin and the canyon that drains the basin during the evening of 15–16 July 1988. The predicted nocturnal potential temperature and wind profiles are compared to tethersonde measurements made at two different locations. Within the basin, the model reproduces the observed near-surface potential temperatures and the profile at 0500 MST, but the model atmosphere cools too quickly between 2000 and 0100 MST so that the near-surface potential temperature gradient is less than that observed. Both the observed and modeled winds near the surface are light and variable. Within the canyon, the model reproduces the observed maximum wind speed around 2300 MST that corresponds to the largest temperature and pressure gradient between the basin atmosphere and the canyon.

The model predicts that the basin fills with cold air by 2200 MST because the outlet canyon is narrow and does not effectively drain the basin atmosphere. A strong horizontal temperature gradient forms between the basin and the Dolores River valley because the valley is much larger and does not cool as fast as the basin. This temperature gradient gradually diminishes by 0500 MST as the Dolores Valley becomes filled with cold air, reducing the pressure gradient and the wind

speeds within the canyon. Unlike larger basins or well-drained valleys, both the observations and the model indicate that the atmosphere within the Sinbad Basin cools throughout the entire evening. Drainage winds from the higher elevations around Pace Peak flow into the basin during the entire evening as well, but the sidewall flows become weaker after 2300 MST as the stability near the basin floor increases. Then a portion of the drainage winds becomes elevated and flows over the cold air pool and, subsequently, over the eastern rim of the basin. The inflow of air into the basin was not anticipated by W96: they assumed that the sidewall drainage flows resulted from local cooling alone and that downward sinking motion compensated for the mass flux through the canyon. Another unexpected finding was the convergence of the near-surface drainage flows in the southern portion of the basin throughout most of the evening.

Even though the predicted temperature profiles in the center of the basin are not perfect, the model qualitatively captures the observed winds within the basin and the canyon and reproduces the temperature profile at the end of the period quite well. This suggests that the net cooling within the basin during the evening is reasonably simulated so that the numerical results can be used to compute the basin heat budget. When the heat budget is averaged between 2000 and 0500 MST, the heat loss within the basin can be attributed mostly to turbulent diffusion. Radiative flux divergence cools the basin atmosphere to a lesser extent overall than turbulent diffusion, while advection produces warming. Turbulent diffusion and advection are both very large over the basin sidewalls, but the cooling due to turbulent diffusion is usually larger than advective warming in those areas. Turbulent diffusion becomes nearly zero in the middle of the basin and cooling in this region results from horizontal advection of cold air from the sidewalls and radiative cooling. Radiative flux divergence did not vary significantly across the basin unless variable surface characteristics were employed. The complex flow field predicted by the model greatly complicates the cooling rate at any one location within the basin; nevertheless, the average heat storage term across the basin is almost directly proportional to the underlying terrain elevation.

Interestingly, the relative contributions of the terms in Eq. (3) are approximately the same for both the model heat budget and the observational heat budget described by W96; however, the magnitudes of the terms are significantly different. One reason for the differences is that sidewall effects cannot be included in the method used by W96 since there were no observations made along the basin sidewalls. On the other hand, the drainage flows produced by the model along the sidewalls cannot be verified either. Forecast errors at the basin site would also account for some of the differences in the methods. The results from this study and W96 suggest that a basin heat budget based on single point measurements can contain relatively large uncertainties in the magnitude of the individual heat budget terms due to an inadequate representation of advection and the failure to resolve the slope flows.

Wind direction had a profound effect on the nocturnal cooling. Since the higher terrain west of the basin can be a major source of cold air, the ambient wind direction affects the amount of cold air that eventually drains into the basin. The acceleration of the ambient winds by the geometry of the underlying terrain will also affect the horizontal and vertical temperature advection within the basin. The model indicates that the presence of vegetation may be important in producing details in the wind and temperature fields at specific locations, as well as affecting the overall basin heat budget. A more complex treatment of vegetation, such as a canopy parameterization, is probably necessary to adequately describe the generation of turbulence and the cooling due to turbulent diffusion along the sidewalls. Still, the vegetation distributions employed in this study had a relatively minor impact on the basin heat budget when compared to the ambient wind direction.

Few three-dimensional dynamic model evaluations, such as the one in this study, have been made using observations from a small-scale basin. While the performance of the model is encouraging, the differences between the model results and the observations demonstrate the difficulty in simulating the evolution of the nocturnal stable boundary layer within small-scale basins. Despite the preliminary results from the tests described in this study, improvements in the forecasts may be achieved with higher spatial resolutions and/or improved parameterizations of nocturnal turbulence in complex terrain. An adequate representation of nocturnal turbulence in complex terrain is especially important since the turbulent diffusion is the dominant cooling mechanism in relatively small basins. A better understanding of basin meteorology is also important for air pollution applications since many urban areas are located within basins.

Acknowledgments. The authors thank Drs. Chris Doran and Rich Barchet for their comments on this manuscript. This research was supported by the Environmental Sciences Division of the U.S. Department of Energy under Contract DE-AC06-76RLO 1830 at Pacific Northwest National Laboratory under the auspices of the Atmospheric Studies in Complex Terrain program. Pacific Northwest National Laboratory is operated by Battelle Memorial Institute for the U.S. Department of Energy.

REFERENCES

Bader, D. C., and T. W. Horst, 1990: Model evaluation of the assumptions used in valley energy budgets. Preprints, *Fifth Conf. on Mountain Meteorology,* Boulder, CO, Amer. Meteor. Soc., 277–280.

——, and ——, 1992: Scale analysis of the thermal energy budget in an idealized mountain valley. Preprints, *Sixth Conf. on Mountain Meteorology,* Portland, OR, Amer. Meteor. Soc., 243–247.

Blockley, J. A., and T. J. Lyons, 1994: Airflow over a two-dimensional escarpment. III: Nonhydrostatic flow. *Quart. J. Roy. Meteor. Soc.,* **120,** 79–109.

Chen, C., and W. R. Cotton, 1983: A one-dimensional simulation of the stratocumulus-capped mixed layer. *Bound.-Layer Meteor.,* **25,** 289–321.

Clements, W. E., J. A. Archuleta, and P. H. Gudiksen, 1989: Experimental design of the 1984 ASCOT field study. *J. Appl. Meteor.,* **28,** 405–413.

Dickinson, R. E., A. Henderson-Sellers, P. J. Kennedy, and M. F. Wilson, 1986: Biosphere–Atmosphere Transfer Scheme (BATS) for the NCAR Community Climate Model. NCAR Tech. Note NCAR/TN-275+STR, National Center for Atmospheric Research, Boulder, CO, 69 pp.

Doran, J. C., 1991: The effects of ambient winds on valley drainage flows. *Bound.-Layer Meteor.,* **55,** 177–189.

Fast, J. D., 1995: Mesoscale modeling in areas of highly complex terrain. *J. Appl. Meteor.,* **34,** 2762–2782.

Helfand, H. M., and J. C. Labraga, 1988: Design of a nonsingular level 2.5 second-order closure model for the prediction of atmospheric turbulence. *J. Atmos. Sci.,* **45,** 113–132.

Horst, T. W., K. J. Allwine, and C. D. Whiteman, 1987: A thermal energy budget for nocturnal drainage flow in a simple valley. Preprints, *Fourth Conf. on Mountain Meteorology,* Seattle, WA, Amer. Meteor. Soc., 15–19.

Legg, B. J., and M. Raupach, 1982: Markov chain simulation of particle dispersion in inhomogeneous flows: The mean drift velocity induced by a gradient in Eulerian velocity variance. *Bound.-Layer Meteor.,* **24,** 3–13.

Louis, J.-F., 1979: A parametric model of vertical eddy fluxes in the atmosphere. *Bound.-Layer Meteor.,* **17,** 187–202.

Mahrer, Y., and R. A. Pielke, 1987: A numerical study of the airflow over irregular terrain. *Contrib. Atmos. Phys.,* **50,** 89–113.

Mellor, G. L., and T. Yamada, 1982: Development of a turbulent closure model for geophysical fluid problems. *Rev. Geophys. Space Phys.,* **20,** 851–875.

Petkovsek, Z., 1978: Zones of convergence in local air flow in valleys and basins. Preprints, *15 Internationale Tagung Fuer Alpine Meteorologie,* Grindelwald, Switzerland, Swiss Meteor. Inst., 92–96.

Pielke, R. A., and Coauthors, 1992: A comprehensive meteorological modeling system—RAMS. *Meteor. Atmos. Phys.,* **49,** 69–91.

Pitts, R. O., and T. J. Lyons, 1989: Airflow over a two-dimensional escarpment. I: Observations. *Quart. J. Roy. Meteor. Soc.,* **115,** 965–981.

Poulos, G. S., and J. E. Bossert, 1995: An observational and prognostic numerical investigation of complex terrain dispersion. *J. Appl. Meteor.,* **34,** 650–669.

Whiteman, C. D., T. B. McKee, and J. C. Doran, 1996: Boundary layer evolution within a canyonland basin. Part I: Mass, heat, and moisture budgets from observations. *J. Appl. Meteor.,* **35,** 2145–2161.

Zhong, S., and C. D. Whiteman, 1995: A numerical study of atmospheric heat budget terms over idealized valley topography. Preprints, *Seventh Conf. on Mountain Meteorology,* Breckenridge, CO, Amer. Meteor. Soc., 339–344.